Supporting Information (SI)

Interfacial electronic engineering of $Ni_3ZnC_{0.7}$/Ni heterostructure embedded in N-doped carbon nanotubes for efficient alkaline electrocatalytic hydrogen evolution

Liangliang Feng[a,b*], Hongyan Yin[a], Changle Fu[a], Lina Dai[c], Yonghui Zhang[c], Liyun Cao[a], Yuhang Li[a], Dan Zhao[a], Yajie Xie[a], Jianfeng Huang[a,b*]

[a] *School of Materials Science & Engineering, Shaanxi Key Laboratory of Green Preparation and Functionalization for Inorganic Materials, Shaanxi University of Science & Technology, Xi'an Shaanxi, 710021, P.R. China.*

[b] *Shaanxi Collaborative Innovation Center of Industrial Auxiliary Chemistry & Technology, Key Laboratory of Auxiliary Chemistry and Technology for Chemical Industry, Ministry of Education, Shaanxi University of Science & Technology, Xi'an Shaanxi 710021, P.R. China.*

[c] *Xi'an Chao Ma Technology Co. Ltd, Xi'an Shaanxi, 710025, P.R. China.*

[*] Corresponding authors.

E-mail addresses: fengll@sust.edu.cn (L. Feng); huangjf@sust.edu.cn

1 Experimental

1.1 Chemicals and materials

All chemicals in this work were of analytical grade and employed directly without further purification. Nickel chloride hexahydrate ($NiCl_2 \cdot 6H_2O$, ≥97.0%), Zinc acetate dihydrate ($Zn(OAc)_2 \cdot 2H_2O$, ≥97.0%) and absolute ethanol (CH_3CH_2OH, ≥99.7%) were procured from Sinopharm (China). Dicyandiamide ($C_2H_4N_4$, ≥99.0%) was obtained from Damao Chemical Reagent Co., Ltd. (China). Platinum on activated carbon (25 wt% Pt/C) was purchased from Shanghai Hesen Electric Co., Ltd. (China). Ultrapure water (>18.2 MΩ cm) was supplied with a PALL PURELAB Plus instrument during the whole experiments.

1.2 Materials characterization.

Phase composite and crystallinity of as-fabricated materials were collected by analyzing the X-ray diffraction (XRD) patterns that performing on a Rigaku D/max 2200PC instrument with Cu Kα radiation source (λ = 0. 15406 nm). Morphologic characteristic and element distribution were identified using the field emission scanning electron microscope (FESEM, Hitachi S-4800) and transmission electron microscope (TEM, FEI Tecnai G2). Surface chemical composition and bonding configuration were characterized by X-ray photoelectron spectrometer (XPS) that implementing on the Axis Ultra Supra equipment with Al K_α radiation.

1.3 Electrochemical measurements.

In this study, all electrochemical tests were carried out on CHI 660E electrochemical workstation (ChenHua Instrument, Inc., Shanghai) by employing a standard three-electrode configuration in 1.0 M KOH electrolyte. Wherein the catalysts-coated glassy carbon electrode (GCE), saturated calomel electrode (SCE, $Hg/HgCl_2$) and carbon rod were employed as the working electrode, reference electrode and counter electrode, respectively. All the potentials converted in accordance with the reference reversible

hydrogen electrode (RHE) basing on the classical Nernst equation ($E_{vs\ RHE} = E_{vs\ SCE} + 0.059 \times pH + 0.2415$ V). Polarization curves were recorded basing on Linear sweep voltammetry (LSV) with 85%-*iR* correction, together with the scanning sweep of 5 mV s^{-1}. Electrochemical impedance spectroscopy (EIS) was measured with an overpotential of 200 mV when the frequency scope was ranging from 1×10^{-2} Hz to 1×10^{5} Hz. Electrochemical active surface areas (ECSA) were evaluated by collecting the cyclic voltammetry (CV) at different scanning rate within the scope of 10 to 120 mV s^{-1} in non-Faraday zone. Further, the electrochemical double-layer capacitance (C_{dl}) was equivalent to the half of fitting straight line slope between the current density difference (Δj) and various sweep rates. The I-t curve expressed the current fluctuation relationship with hydrogen production reaction time under the condition of constant potential.

1.4 Theoretical calculation:

All DFT calculation were constructed and implemented in the Vienma ab initio simulation package (VASP).[1,2] Using the electron exchange and correlation energy was treated within the generalized gradient approximation in the Perdew−Burke−Ernzerhof functional (GGA-PBE) and the calculations were done with a plane-wave basis set defined by a kinetic energy cutoff of 450 eV.[3] The k-point sampling was obtained from the Monkhorst−Pack scheme with a (3 × 3 × 1) mesh for optimization and electronic structure of Ni(111) and $Ni_3ZnC_{0.7}$(100) and with (1 × 3 × 1) of optimization and electronic structure of $Ni_3ZnC_{0.7}$(100)/Ni(111). The geometry optimization and energy calculation are finished when the electronic self-consistent iteration and force were reach 10^{-5} eV and 0.02 eV $Å^{-1}$, respectively.

The HER process is divide into the four fundamental reactions as following：

（1） $H+ + e^- + * = *H$

（2） $*H = * + 1/2\ H_2$

*H presents the H moiety on the adsorption site. Where which the energy of H^+/e^- is approximately equal to the energy of 1/2 H_2.[4]

(1) The Gibbs Free Energy Variation

The change in Gibbs free energy (△G) of each adsorbed intermediate was calculated

based on the computational hydrogen electrode method developed by Nørskov et al.8 At standard condition (T = 298.15 K, pH = 0, and U = 0 V (vs. SHE)), the free energy G is defined as the following equation:

$$\triangle G = \triangle E + \triangle E_{ZPE} - T\triangle S$$

Where $\triangle$E is the energy change obtained from DFT calculation, $\triangle E_{ZPE}$ is the difference between the adsorbed state and gas, which was calculated by summing vibrational frequency for all model based on the equation: $E_{ZPE} = 1/2\sum h\nu_i$ (. T is the temperature (298.15 K) in the above reaction system, and $\triangle$S represents the difference on the entropies between the adsorbed state and gas phase. The entropies of free molecules were obtained from NIST database (https://janaf.nist.gov/). And the free energy of the adsorbed state *H can be taken as: $\triangle G_{*H}=\triangle E_{*H}+0.24$.[5]

(2) d-band center

The d-band center proposed by Nørskov and co-workers is a semi-quantitative descriptor to describe the trend of reactivity of transition metals (TM), which is defined the *d*-band center (ε_d) relative to the Fermi level (E_F).[6] A transition metal with a low ε_d value relative to the Fermi level, shows a weak adsorption for a given adsorbate. And the *d*-band center (ε_d) is calculated as following：

$$\varepsilon_d = \frac{\int_{-\infty}^{+\infty} x\rho(x)\mathrm{d}x}{\int_{-\infty}^{+\infty} \rho(x)\mathrm{d}x}$$

Where ρ(x) is the projector density of states (PDOS) with respect to Ni atoms in Ni(111), $Ni_3ZnC_{0.7}$(100) and $Ni_3ZnC_{0.7}$(100)/Ni(111).

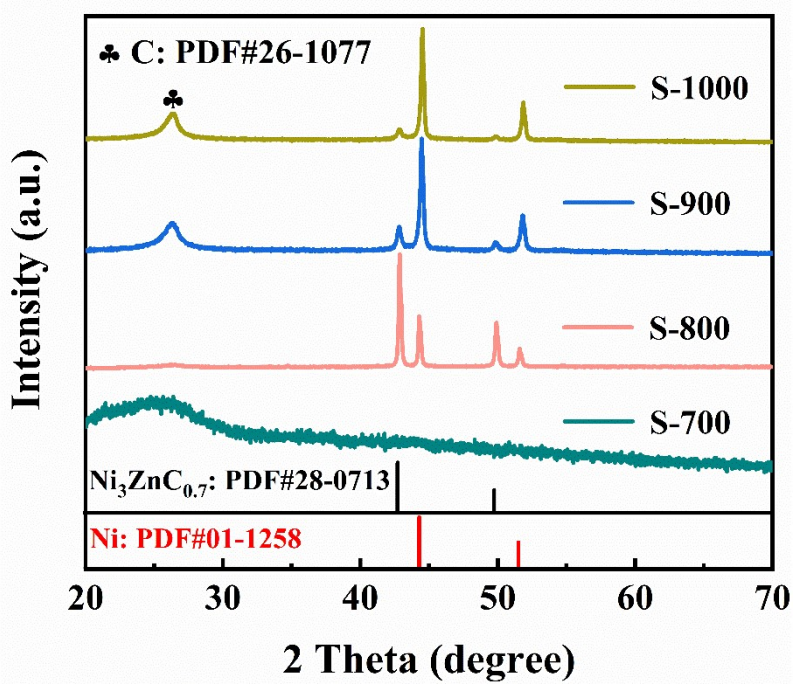

Fig. S1 XRD patterns of S-700, S-800, S-900 and S-1000 catalysts.

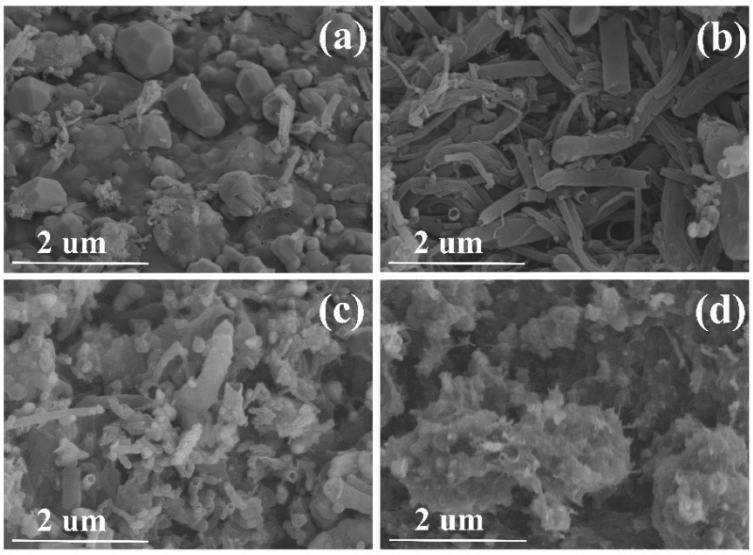

Fig. S2 SEM images of (a) S-700, (b) S-800, (c) S-900 and (d) S-1000 samples.

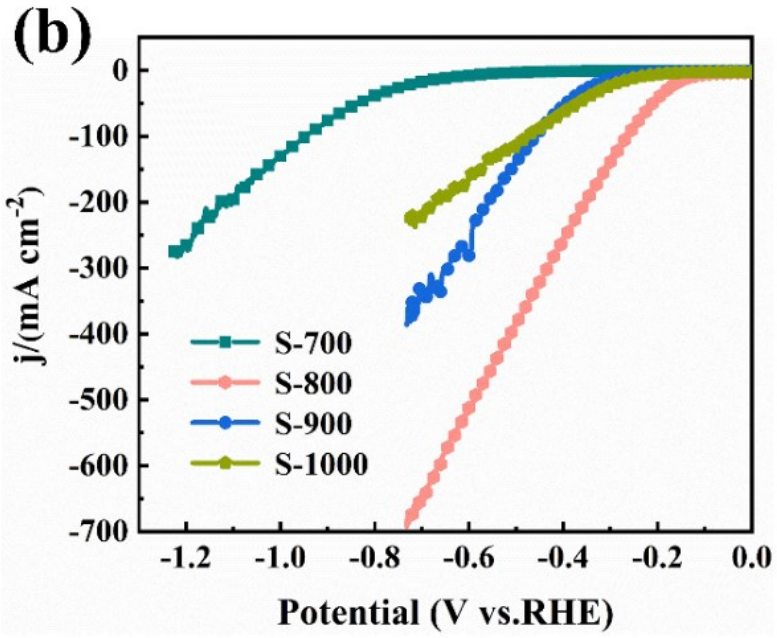

Fig. S3 LSV curves of S-700, S-800, S-900 and S-1000 catalysts.

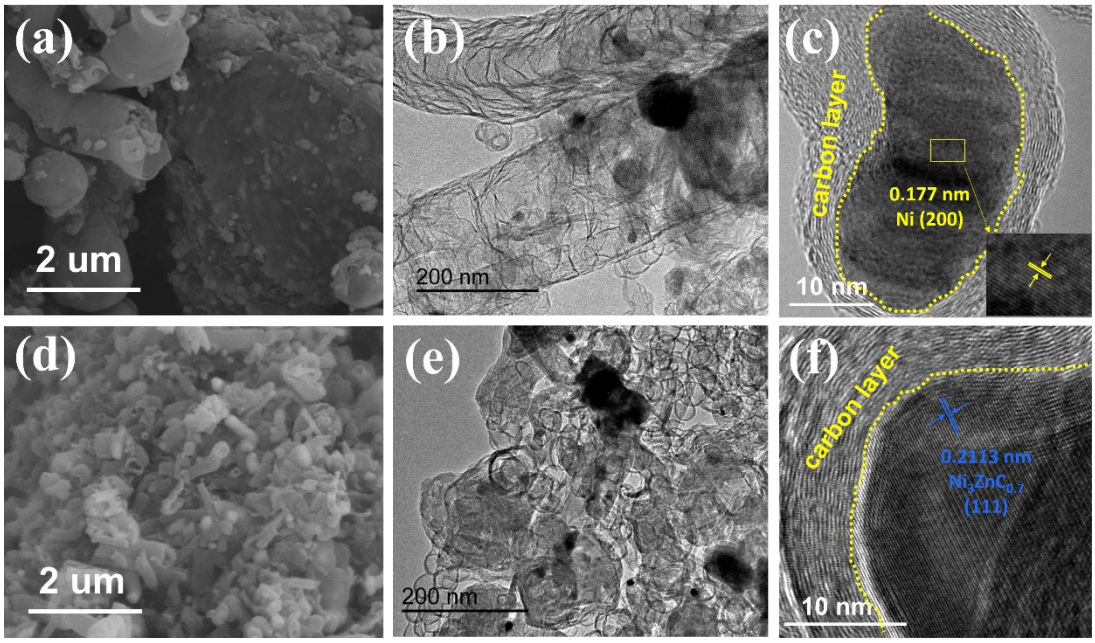

Fig. S4 (a) SEM image, (b) TEM image and (c) HRTEM image of Ni@CNTs; (d) SEM image, (b) TEM image and (c) HRTEM image of $Ni_3ZnC_{0.7}$@CNTs.

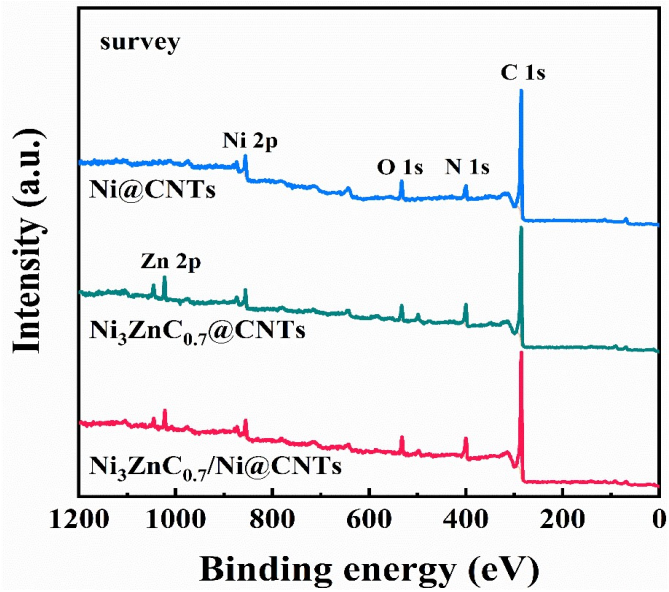

Fig. S5 XPS spectra for the survey scan of Ni@CNTs, $Ni_3ZnC_{0.7}$@CNTs and $Ni_3ZnC_{0.7}$/Ni@CNTs.

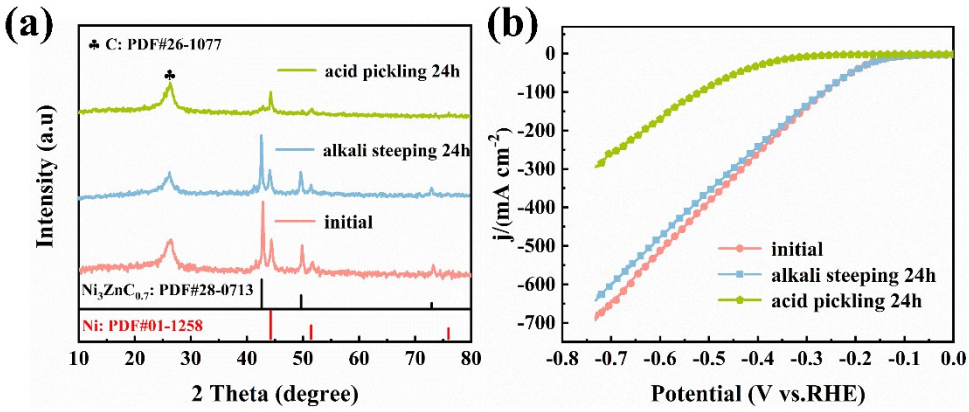

Fig. S6 XRD (a) and LSV curves (b) of the sample after acid and alkali treatment.

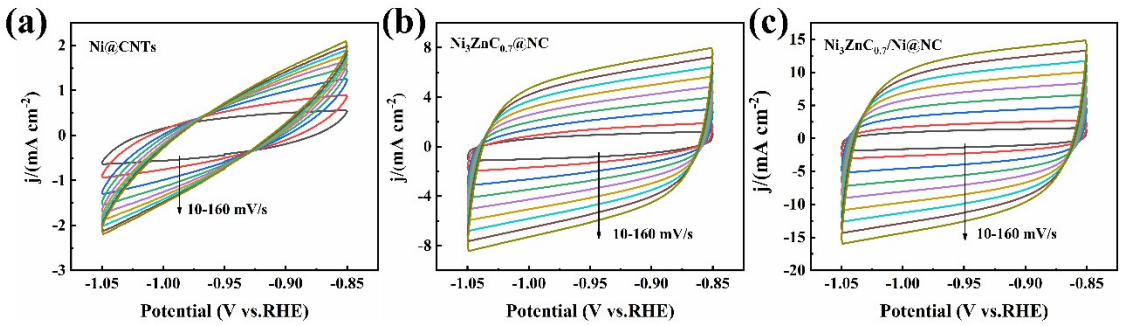

Fig. S7 Cyclic voltammograms of (a) Ni@CNTs, (b) $Ni_3ZnC_{0.7}$@CNTs and (c) $Ni_3ZnC_{0.7}$/Ni@CNTs.

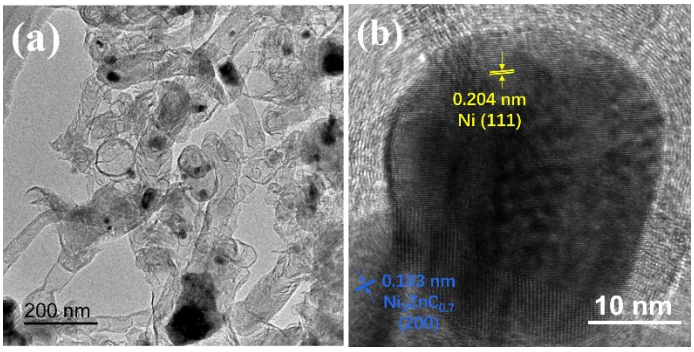

Fig. S8. Structure characterization of $Ni_3ZnC_{0.7}$/Ni@CNTs after 2000 cycle CV in 1M KOH: (a) TEM image and (b) HRTEM image.

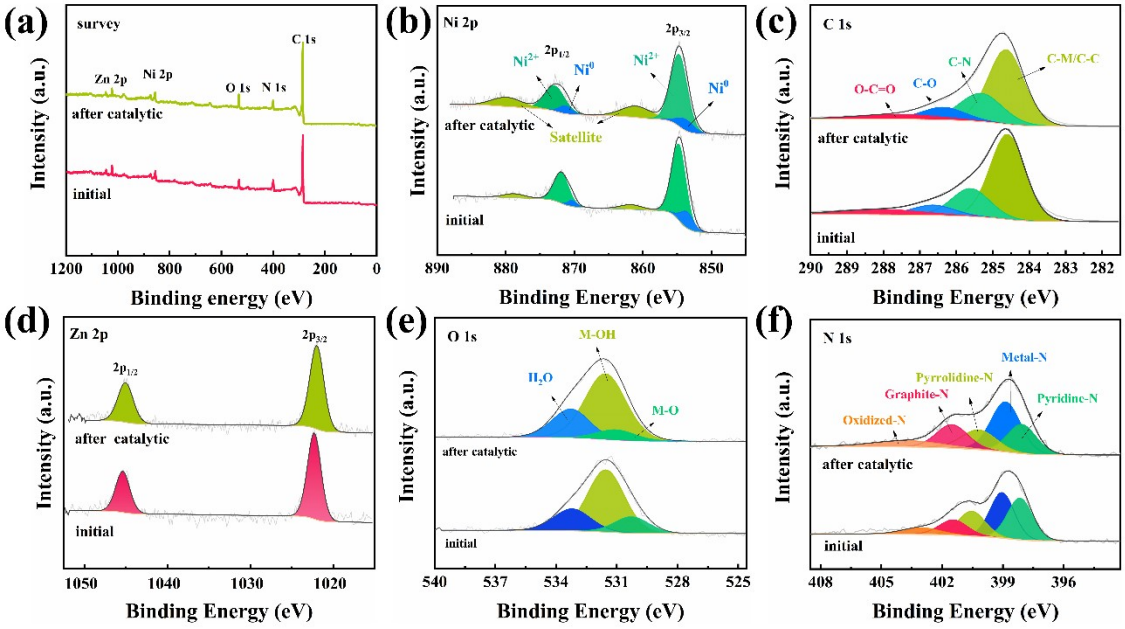

Fig. S9 XPS spectra for survey (a), Ni 2p (b), C 1s (c), Zn 2p (d), O 1s (e) and N 1s (f) of the $Ni_3ZnC_{0.7}$/Ni@CNTs before and after 400h i-t test in 1M KOH solutions.

Table S1 Proportional distribution of different binding type of N for Ni@CNTs, $Ni_3ZnC_{0.7}$@CNTs and $Ni_3ZnC_{0.7}$/Ni@CNTs.

N types	Ni@CNTs	$Ni_3ZnC_{0.7}$@CNTs	$Ni_3ZnC_{0.7}$/Ni@CNTs
Pyridine-N	12.82%	32.7%	29.76%
Metal-N	39.53%	32.08%	31.43%
Pyrrolidine-N	18.31%	17.97%	19.05%
Graphite-N	20.82%	11.67%	12.42%
Oxidized-N	8.53%	5.58%	7.43%

Table S2 The performance comparision of this thesis and recently published bimetallic carbide based electrocatalysts.

catalyst	electrolyte	η[mV]@j[mA cm^{-2}]	Durability	Ref.
$Ni_3ZnC_{0.7}$/Ni@CNTs	1M KOH	93@10	500 h	In this work
$Mo_xW_{2-x}C$@C	1M KOH	106@10	20h	[7]
$Co_{0.31}Mo_{1.69}C$/MXene/NC	1M KOH	251@10	225h	[8]
$Ni_3ZnC_{0.7}$/NCNT-700	1M KOH	203@10	24h	[9]
Fe_3W_3C NRs/RGO	1M KOH	77@10	10,000 cycles	[10]
$Co_6Mo_6C_2$@NCNT-800	1M KOH	122.14@10	24h	[11]
N-Co_6Mo_6C	1M KOH	161@10	20h	[12]
$Mo_xW_{2-x}C$/N, P-codop CNTs	1M KOH	145@10	50h	[13]
Ni_3Mo_3C/Mo_2C/Ti_3C_2Tx/NC	1M KOH	98@10	24h	[14]
$Mo_{1.33}W_{0.67}C$ @ NC	1M KOH	108@10	40h	[15]
Co_3Mo_3C/Co@NC	1M KOH	68@10	20h	[16]
Co_3Mo_3C	1M KOH	169@10	15h	[17]
$Co_6Mo_6C_2$/$Co_2Mo_3O_8$	1M KOH	220@10	12h	[18]
Mo_2C/Mo_3Co_3C-NF-2	1M KOH	87@10	5000 cycles	[19]
Ni_3Mo_3C@NPC NWs/CC	1M KOH	215@100	48h	[20]

References

[1] Kresse, G.; Furthmüller, J. Efficiency of ab-initio total energy calculations for metals and semiconductors using a plane-wave basis set. *Computational Materials Science* **1996**, *1*(6), 15-50, DOI: 10.1016/0927-0256(96)00008-0;

[2] Kresse, G.; Furthmüller, J. Efficient iterative schemes for *ab initio* total-energy calculations using a plane-wave basis set. *Physical Review B* **1996**, *54*, 11169, DOI: 10.1103/PhysRevB.54.11169;

[3] Ernzerhof, M.; Perdew, J. P. Generalized gradient approximation to the angle- and system-averaged exchange hole. *J. Chem. Phys.* **1998**, *109*, 3313–3320, DOI: 10.1063/1.476928;

[4] Nørskov, J. K.; Rossmeisl, J.; Logadottir, A.; Lindqvist, L.; Kitchin, J. R.; Bligaard, T.; Jónsson, H. Origin of the overpotential for oxygen reduction at a fuel-cell cathode. *J. Phys. Chem. B* **2004**, *108*, 46, 17886–17892, DOI: 10.1021/jp047349j;

[5] Nørskov, J. K.; Bligaard, T.; Logadottir, A.; Kitchin, J. R.; Chen, J. G.; Pandelov, S.; Stimming, U. Trends in the exchange current for hydrogen evolution. *J. Electrochem. Soc.* **2005**, *152*, J23, DOI: 10.1149/1.1856988.

[6] Nørskov, J. K.; Abild-Pedersen, F.; Studt, F.; Bligaard, T. Density functional theory in surface chemistry and catalysis. *PNAS* **2011**, *108* (3), 937-943, DOI: 10.1073/pnas.1006652108;

[7] Lin, L.; Chen, M.; Wu, L. Synthesis of Molybdenum-Tungsten Bimetallic Carbide Hollow Spheres as pH-Universal Electrocatalysts for Efficient Hydrogen Evolution Reaction. *Advanced Materials Interfaces* **2018,** *5* (23), DOI: 10.1002/admi.201801302.

[8] Wu, X.; Zhou, S.; Wang, Z.; Liu, J.; Pei, W.; Yang, P.; Zhao, J.; Qiu, J. Engineering Multifunctional Collaborative Catalytic Interface Enabling Efficient Hydrogen Evolution in All pH Range and Seawater. *Advanced Energy Materials* **2019,** *9* (34), DOI: 10.1002/aenm.201901333.

[9] Li, R.; Li, X.; Yu, D.; Li, L.; Yang, G.; Zhang, K.; Ramakrishna, S.; Xie, L.; Peng, S. $Ni_3ZnC_{0.7}$ nanodots decorating nitrogen-doped carbon nanotube arrays as a self-standing bifunctional electrocatalyst for water splitting. *Carbon* **2019,** *148*, 496-503, DOI: 10.1016/j.carbon.2019.04.002.

[10] He, C.; Bo, T.; Wang, B.; Tao, J. RGO induced one-dimensional bimetallic carbide nanorods: An efficient and pH-universal hydrogen evolution reaction electrocatalyst. *Nano Energy* **2019,** *62*, 85-93, DOI: 10.1016/j.nanoen.2019.05.009.

[11] Feng, X.; Bo, X.; Guo, L. An advanced hollow bimetallic carbide/nitrogen-doped carbon nanotube for efficient catalysis of oxygen reduction and hydrogen evolution and oxygen evolution reaction. *Journal of Colloid and Interface Science* **2020,** *575*, 69-77, DOI: 10.1016/j.jcis.2020.04.093.

[12] Geng, S.; Xu, S.; Yu, Y. S.; Yang, W.; Feng, M.; Li, H. N-doped Co6Mo6C nanorods as highly active and durable bifunctional electrocatalysts for water splitting. *Journal of Electroanalytical Chemistry* **2020,** *871*, DOI: 10.1016/j.jelechem.2020.114271.

[13] Zhao, Z.; Zhu, Z.; Wang, F.; Li, S.; Bao, X.; Zhang, L.; Lin, S.; Yang, Y. Bimetallic carbides embedded in heteroatom-doped carbon nanotubes for efficient electrocatalytic hydrogen evolution reaction and high-performance lithium storage. *Chemical Engineering Journal* **2021,** *415*, DOI: 10.1016/j.cej.2021.128885.

[14] Xu, C.; Wu, F.; Yang, X.; Feng, K.; Zhang, M.; Wang, Y.; Yang, L.; Jiang, N.; Yin, S. Synergistically coupling of $Ni_3Mo_3C/Mo_2C/Ti_3C_2T_x$ MXene/N-doped carbon electrocatalyst towards enhanced hydrogen evolution activity. *Journal of Alloys and Compounds* **2022,** *920*, DOI: 10.1016/j.jallcom.2022.165826.

[15] Li, H.; Hu, M.; Zhang, L.; Huo, L.; Jing, P.; Liu, B.; Gao, R.; Zhang, J.; Liu, B. Hybridization of Bimetallic Molybdenum-Tungsten Carbide with Nitrogen-Doped Carbon: A Rational Design of Super Active Porous Composite Nanowires with Tailored Electronic Structure for Boosting Hydrogen Evolution Catalysis.

Advanced Functional Materials **2020,** *30* (40), DOI: 10.1002/adfm.202003198.

[16] Gao, S.; Lin, L.; Wang, H.; Nie, P.; Jian, J.; Li, J.; Chang, L. Synergistic effect of Co_3Mo_3C and Co in N-doped carbon for efficient overall water splitting. *Journal of Alloys and Compounds* **2021,** *875*, DOI: 10.1016/j.jallcom.2021.160052.

[17] Gao, S.; Chen, H.; Liu, Y.; Li, G.-D.; Gao, R.; Zou, X. Surface- clean, phase-pure multi- metallic carbides for efficient electrocatalytic hydrogen evolution reaction. *Inorganic Chemistry Frontiers* **2019,** *6* (4), 940-947, DOI: 10.1039/c8qi01360h.

[18] Liu, R.; Anjass, M.; Greiner, S.; Liu, S.; Gao, D.; Biskupek, J.; Kaiser, U.; Zhang, G.; Streb, C. Bottom-up Design of Bimetallic Cobalt-Molybdenum Carbides/Oxides for Overall Water Splitting. *Chemistry-a European Journal* **2020,** *26* (18), 4157-4164, DOI: 10.1002/chem.201905265.

[19] Wang, Y.-Q.; Xie, Y.; Zhao, L.; Sui, X.-L.; Gu, D.-M.; Wang, Z.-B. Hierarchical Heterostructured Mo_2C/Mo_3Co_3C Bouquet-like Nanowire Arrays: An Efficient Electrocatalyst for Hydrogen Evolution Reaction. *Acs Sustainable Chemistry & Engineering* **2019,** *7* (7), 7294-7303, DOI: 10.1021/acssuschemeng.9b00358.

[20] Guo, L.; Wang, J.; Teng, X.; Liu, Y.; He, X.; Chen, Z. A Novel Bimetallic Nickel-Molybdenum Carbide Nanowire Array for Efficient Hydrogen Evolution. *Chemsuschem* **2018,** *11* (16), 2717-2723, DOI: 10.1002/cssc.201801110.